### Title

Thermodynamically Driven Synthetic Optimization for Cation-Disordered Rock Salt Cathodes




### Journal

Advanced Energy Materials, 12(21)

### ISSN

1614-6832



### Authors

Cai, Zijian
Zhang, Ya-Qian
Lun, Zhengyan
et al.



### Publication Date

2022-06-01

### DOI

10.1002/aenm.202103923

**Thermodynamically driven synthetic optimization for cation-disordered rocksalt cathodes**

*Zijian Cai[†], Ya-Qian Zhang[†], Zhengyan Lun[†*], Bin Ouyang, Leighanne C. Gallington, Yingzhi Sun, Han-Ming Hau, Yu Chen, Mary C. Scott[*], Gerbrand Ceder[*]*

Z. Cai, Dr. Y.-Q. Zhang, Dr. Z. Lun, Dr. B Ouyang, Y. Sun, H.-M. Hau, Y. Chen, Prof. M. C. Scott, Prof. G. Ceder
Department of Materials Science and Engineering
UC Berkeley
Berkeley, CA 94720, USA

Z. Cai, Dr. Z. Lun, Dr. B Ouyang, Y. Sun, H.-M. Hau, Y. Chen, Prof. G. Ceder
Materials Sciences Division
Lawrence Berkeley National Laboratory
Berkeley, CA 94720, USA

Dr. Y.-Q. Zhang, Prof. M. C. Scott,
National Center for Electron Microscopy
Molecular Foundry
Lawrence Berkeley National Laboratory
Berkeley, CA 94720, USA

Dr. Z. Lun
Department of Chemistry
University of Chinese Academy of Sciences
Beijing, 100049, China

Dr. L. C. Gallington
X-ray Science Division
Advanced Photon Source
Argonne National Laboratory
Argonne, IL 60439, USA

[†] These authors contributed equally.
Email: zylun@ucas.ac.cn, mary.scott@berkeley.edu, gceder@berkeley.edu

**Abstract**

Relating the synthesis conditions of materials to their functional performance has long been an experience-based trial-and-error process. However, this methodology is not always efficient in identifying an appropriate protocol and can lead to overlooked opportunities for the performance optimization of materials through simple modifications of the synthesis process. In this work, we systematically track the structural evolution in the synthesis of a representative disordered rocksalt (a promising next-generation Li-ion cathode material) at the scale of both the long-range crystal structure and the short-range atomic structure using various *in situ* and *ex situ* techniques, including transmission electron microscopy, X-ray diffraction, and pair distribution function analysis. An optimization strategy is proposed for the synthesis protocol, leading to a remarkably enhanced capacity (specific energy) of 313 mAh $g^{-1}$ (987 Wh $kg^{-1}$) at a low rate (20 mA $g^{-1}$), with a capacity of more than 140 mAh $g^{-1}$ retained even at a very high cycling rate of 2,000 mA $g^{-1}$. This strategy is further rationalized using *ab initio* calculations, and important opportunities for synthetic optimization demonstrated in this study are highlighted.

## 1. Introduction

While composition and structure are typical design handles to modify the properties of materials, it is well established that attributes regulated by the synthesis of a material may also control materials performance in a substantial way. This can include shape and morphology, defects, microstructure, secondary structural variations, etc. How these modify performance depends on the specific properties of interest, but general optimization of these secondary structural features through synthesis is often a process of trial-and-error, with a certain degree of guidance provided by experiment or density functional theory (DFT)-based phase diagram calculation.[1] Such a "black box" approach to capture the relation between synthesis, products and performance is slow and can miss opportunities to enhance materials properties simply through modifications of the synthesis procedure. Recent advances in the *in situ* observation of materials synthesis foster enhanced understanding towards how it can be controlled by synthesis parameters.[2, 3, 4, 5] While most *in situ* synthesis studies performed to date have focused on the phase changes in the synthesis process of the ceramic material itself, we demonstrate in this paper that a more systematic approach can be taken through the convergence of theory and high-resolution characterization methods to relate structural details and performance. Specifically, *in situ* characterization of the synthesis of disordered-rocksalt (DRX) type Li-ion battery cathode materials demonstrates that a crystalline rocksalt forms from the precursors on a very different time scale than the time needed to short-range order the cations in this rocksalt, providing an opportunity for creating DRX materials with enhanced performance by stopping the synthesis early to freeze the material in a metastable state of disorder.

Li-excess DRX materials are a young family of next-generation Li-ion cathode materials, in which there are no well-separated Li or transition metal (TM) sublattices.[6-9] These materials are promising cathode compounds as they remove the dependence on Co and Ni [9, 10], crucial to maintain the structure in layered cathode materials.[11] The performance of DRX materials is strongly connected to details of their structure through the statistics of the local cation environments that form in the structure upon synthesis: Li ions migrate through a percolating network of tetrahedral 0-TM units where a lack of TM presence around the activated state facilitates migration of Li through the tetrahedral site.[6, 12] However, DRX cathodes can suffer from poor rate capability when unfavorable local short-range order (SRO) which reduces the amount of 0-TM environments is present.[9, 13, 14, 15] SRO has been proven to be crucial in controlling the Li transport and thus the capacity and rate capability in DRX cathodes, the appropriate manipulations of which can lead to significant enhancement of the electrochemical performance.[16, 17]

We selected a representative DRX composition of $Li_{1.2}Mn_{0.55}Ti_{0.25}O_{1.85}F_{0.15}$ (LMTF), consisting of earth-abundant and inexpensive transition metals and tracked the structure, especially the generation and evolution of the SRO during the synthesis, using a combination of *in situ* and *ex situ* characterization techniques, including transmission electron microscopy (TEM) electron diffraction (ED), X-ray diffraction (XRD), and synchrotron pair distribution function (sPDF) analysis. It is observed that while the long-range DRX structure forms rapidly during synthesis, the generation of SRO occurs over a longer time scale, enabling us to obtain DRX compounds with identical composition but different degrees of SRO by controlling the sintering time at high temperature. Specifically, LMTF sintered at 1000 °C for 35 min [denoted as LMTF (35 min)]

displays significantly less SRO than LMTF sintered for 4 h [denoted as LMTF (4 h)], and consequently, LMTF (35 min) exhibits greatly enhanced electrochemical performance in terms of both capacity (specific energy) and rate capability as compared to LMTF (4 h). First-principles calculations are used to clarify the very different timescale for rocksalt and short-range order formation. This example highlights the opportunities in the synthetic optimization of functional ceramic materials by combining computation, *in situ* and multi-modal synthesis observation, and structure-property models for the performance of the material.

## 2. *In situ* transmission electron microscopy

TEM ED can detect both the long-range crystal structure and the short-range local ordering in the material and present this information in a visual manner, as demonstrated in previous studies. [14, 18] Here, we adopted a Protochips Fusion *in situ* heating TEM holder (shown in Fig. 1A) in the transmission electron microscope, which allows us to simultaneously track the evolution of both the long-range order (LRO) and SRO in the same particle *in situ* upon heating by acquiring ED. The heating profile applied in the experiment is shown in Fig. 1B, with red points indicating when an ED pattern was collected on the same particle (except for the 4 h sample, which was collected *ex situ*). In addition, the elemental distribution of Mn and Ti during the ramping process was tracked using scanning transmission electron microscopy (STEM)–energy-dispersive spectroscopy (EDS) mapping. The result, shown in Fig. S1, indicates that the incorporation of the Mn and Ti precursor mainly occurs above 800°C, consistent with previous reports that the synthesis of DRX materials usually requires a high temperature of approximately 1000°C. [8, 9]

The structural evolution within a representative particle was tracked during heating at 1000°C. ED patterns along the [100] zone axis of the particle were acquired at times of 5 min, 15 min, and 35 min, as shown in Fig. 1C–E. The sample that was heated for 4 h at 1000°C was measured *ex situ* (Fig. 1F) due to the change of orientation of the particle upon heating, which moved beyond the tilting limit of the holder to track the same zone axis. In the ED patterns, the round Bragg diffraction spots represent long-range crystal structural information, which can be indexed to the *Fm-3m* space group and originate from the average rocksalt structure in all four patterns. This result suggests that the LRO in the DRX compound forms rather rapidly during the

synthesis and at a relatively low temperature before reaching 1000°C. The square-like diffuse scattering intensities in the ED patterns are attributed to SRO. The intensity of the diffuse scattering can be integrated within the dashed rectangular regions and compared during different stages of the synthesis, as displayed by the intensity profiles next to each ED image. It is clearly observed that the diffuse scattering patterns gradually emerge with sintering time. At 5 min, there is barely any diffuse scattering present; however, as the sample spends more time at 1000°C, the diffuse scattering intensity increases, becoming rather pronounced at 4 h, which is the typical time scale adopted in the synthesis of DRX compounds reported previously.[9, 19] This observation indicates that the SRO formation in DRX compounds is a slow process, in sharp contrast to the formation of LRO, which occurs rapidly.

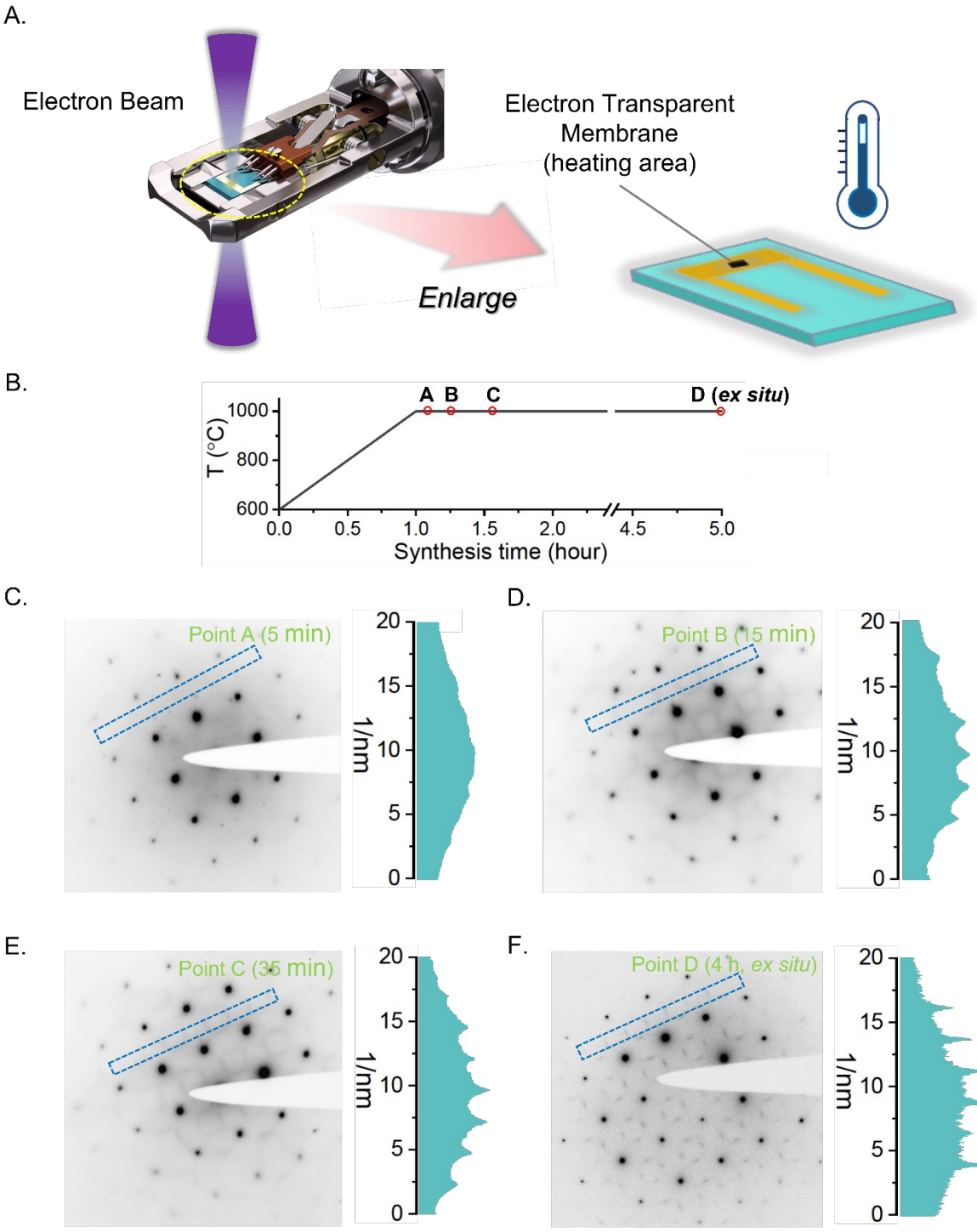


**Figure 1. *In situ* temperature-dependent TEM characterization of the synthesis process of LMTF. (A)** Schematic illustration of the *in situ* temperature-dependent TEM setup. The area of heating with an electron transparent membrane is enlarged. **(B)** Heating profile of pre-heated LMTF 'precursor'. The red circles mark the times at which ED patterns were collected. **(C–E).**

TEM–ED patterns collected on the same particle at different times [**(C)** 5 min; **(D)** 15 min; **(E)** 35 min] along the [100] zone axis. **(F)** TEM–ED pattern of the sample with a sintering time of 4 h collected *ex situ*. The round spots, which originate from the LRO in the materials, are indexed to the Fm-3m space group. The square-like diffuse scattering patterns are attributed to the SRO. Quantifications of the SRO pattern intensity by integrating the counts within the dashed rectangular regions are displayed next to the ED patterns.

### 3. Synchrotron-based characterization

To supplement our TEM observations with more bulk sensitive information regarding the structural evolution upon heating, synchrotron-based XRD and PDF were further performed to analyze the long-range crystal structure and short-range local ordering, respectively. This objective would ideally be achieved via an *in situ* experiment; however, this attempt was unsuccessful because of the reactivity between our materials and the quartz capillaries used as sample holders in the *in situ* flow-cell setup at the beamline.[20] Instead, we probed the LRO and SRO using *ex situ* XRD and PDF by selecting seven points in the synthesis process, focusing on the region of interest at high temperature: ramped to 900°C, ramped to 1000°C (without holding), ramped to 1000°C followed by holding for 5 min, 15 min, 35 min, 1 h, and 4 h. The details of the sample preparation are described in the methodology section.

Fig. 2A presents the synchrotron XRD spectra of the seven samples (marked by red circles on the heating profile shown in Fig. 2C). These results confirm that the rocksalt-type LRO forms rapidly and at a temperature before reaching 900°C. Upon further ramping and sintering at 1000°C, the LRO of the material no longer changes, as demonstrated in the *ex situ* XRD spectra, with no observable peak shift observed for all seven samples. Additional Bragg peaks from unreacted $Li_2CO_3$ and LiF precursors can also be observed in all samples, marked by triangles and asterisks, respectively, which suggests the existence of small amount of $Li_2CO_3$ and LiF impurities ranging from 3~8%. The degree of SRO at different stages of the synthesis was qualitatively evaluated by fitting the synchrotron PDF results at low *r* values (between 1.8 and 15 Å) using a random structure. A smaller $R_w$ factor from the fitting would thus suggest a smaller deviation from a random structure, i.e., less SRO. Fig. 2B presents the fitting results for the samples held for 5-min, 35-min, and 4-h as representatives, with the results for the remainder of

the samples and refined parameters presented in the supplementary information (Fig. S2, Table S1). The $R_w$ factors are summarized in Fig. 2C and demonstrate an overall increasing $R_w$ factor as the holding time at 1000°C increases. Investigating the PDF fit in more detail shows that the largest mismatch between the experiment and fitting for samples held longer occurs at very small $r$ (between 1.8 and 4.5 Å) which originates from the local metal rearrangements to form SRO. The PDF results suggest that SRO in LTMF forms in a comparatively slow manner during the synthesis, which is consistent with our *in situ* TEM observations.

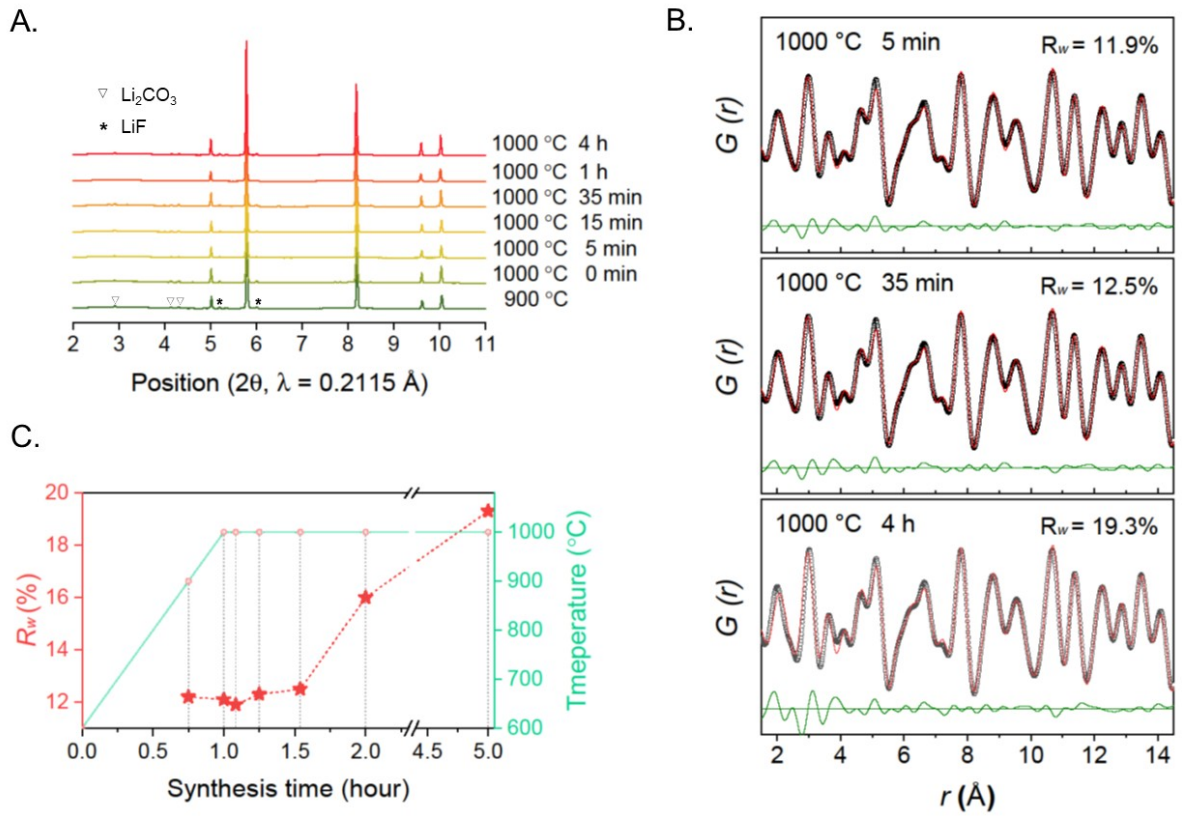


**Figure 2. Synchrotron-based characterization of LMTF at different stages of synthesis. (A)** *Ex situ* XRD results at seven different stages of synthesis: ramped to 900°C, ramped to 1000°C (without holding), and ramped to 1000°C followed by holding for 5 min, 15 min, 35 min, 1 h, and 4 h. Peaks from small amount of unreacted $Li_2CO_3$ and LiF precursors are marked by triangles and asterisks, respectively. **(B)** sPDF fitting results of samples sintered at 1000°C for 5 min (upper panel), 35 min (middle panel), and 4 h (lower panel) using a random structure. The

experimental data are plotted as black open circles, the fittings are plotted as solid red lines, and the difference between observation and calculation is plotted as solid green lines. **(C)** Summary of $R_w$ factors obtained from each PDF fitting at various stages of the synthesis. The synthesis profile is also overlaid, with red circles marking the points of data collection. The grey dashed lines are displayed to guide the eye.

## 4. Computational rationalization

Previous work has shown that thermodynamic driving forces, when evaluated under the appropriate conditions, can rationalize the evolution of phases in a synthesis mixture.[4, 5, 21] We calculated the grand potential of the entire system (open to $CO_2$ release) relative to the precursors in the random rocksalt and the short-range ordered rocksalt. The energy scale was normalized by the number of cations. The random rocksalt was modelled by a special-quasi-random structure with 40 cations (including $Li^+$, $Mn^{3+}$ and $Ti^{4+}$) which maximizes cation randomness in the unit cell. The short-range ordered state and its free energy at 1273 K were determined using the cluster expansion technique as detailed in the Methods section. The results are shown in Figure 3 as blue circles at -5.40 eV/cation for the random rocksalt and at -5.48 eV/cation for the short-range ordered rocksalt, enabling us to sketch a semi-quantitative energetic landscape along the reaction pathway of LMTF.

As Fig. 3 shows, a very large energy decrease is associated with the formation of the random rocksalt from the precursors (−5.4 eV/cation ≈ 522kJ/cation mole) explaining why it may form rapidly and at a relatively low temperature. In contrast, short-range ordering the cations from the random rocksalt into the LMTF with SRO decreases the energy by only about 0.076 eV/cation ( ≈ 7.3kJ/cation mole). This low driving force is likely what is responsible for the long time needed to form SRO. These driving forces revealed by the calculations results are well in line with the experimental observations and indicate a thermodynamic origin of the structural evolution observed during synthesis.

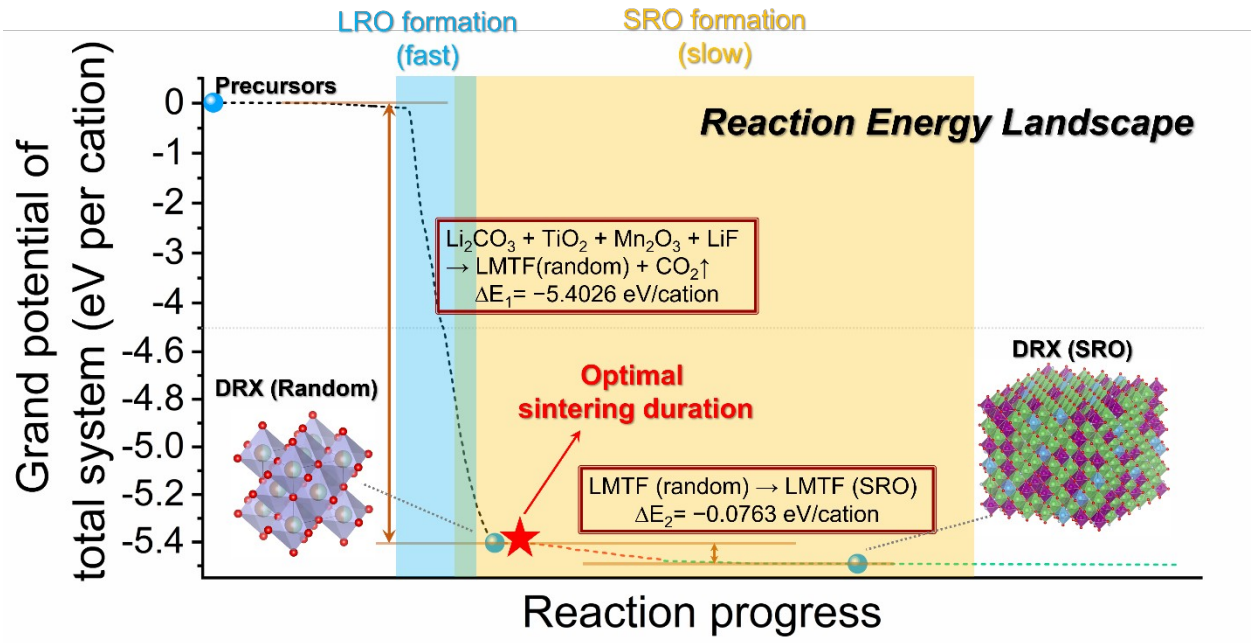


**Figure 3. Schematic of the reaction energy in the LMTF synthesis process.** The grand potential evolution of the total system is computed *ab initio* for the random rocksalt and the short-range ordered rocksalt (simulated at 1273 K), and schematically interpolated (with dashed line). Note that two different energy scales are used (separated at −4.5eV) to highlight the small energy decrease in the SRO formation.

**5. Demonstration of the synthetic optimization strategy**

The different time scales for the formation of the random rocksalt and the short-range ordered structure offers a unique opportunity to optimize the electrochemical performance of the material through modification of its synthesis protocol. Since SRO tends to reduce Li percolation channels and therefore capacity and rate capability in a DRX cathode material [14, 15, 17, 22], we adjusted the synthesis protocol by shortening the sintering time with the objective of obtaining a DRX structure with reduced SRO. We compare the performance of LMTF samples sintered at 1000°C for 35 min [LMTF (35 min)] and 4 h [LMTF (4 h)]. We selected the LMTF (35 min) sample based on the thermogravimetric analysis (shown in Fig. S3) to keep the overall compositions of the two materials as close as possible, as there was almost no observable weight change of the material (<0.5%) after sintering at 1000°C for 35 min. Additional elemental analyses were also conducted (shown in Table S2), which further confirm that LMTF (35 min) and LMTF (4 h) have similar compositions that are close-to-target. Scanning electron microscopy (SEM) and statistical particle size analysis shown in Fig. S4 and S5, respectively, demonstrate that the two samples are similar in terms of particle size both in the as-synthesized state and after the shaker milling used for electrode fabrication. We should thus be able to attribute any difference in electrochemical performance to the different degree of SRO present in the two samples (confirmed *ex situ* as shown in Fig. S6).

The electrochemical performance of the two samples was evaluated using galvanostatic cycling and is shown in Fig. 4. When cycled between 1.5 and 4.8 V at a rate of 20 mA $g^{-1}$, LMTF (35 min) exhibits a very high capacity (specific energy) of 313 mAh $g^{-1}$ (987 Wh $kg^{-1}$) (Fig. 4A), which is significantly larger than that of LMTF (4 h) (273 mAh $g^{-1}$ (852 Wh $kg^{-1}$)) (Fig. 4B).

This finding is consistent with the design principle of DRX materials that the mitigation of unfavorable SRO improves the overall Li transport by forming a better-extended Li percolation network, thus leading to an improved capacity. Further support for the influence of the synthesis time on performance is given by the high rate performance: LMTF (35 min) delivers 143 mAh $g^{-1}$ at a very high rate of 2,000 mA $g^{-1}$ (Fig. 4C), which is more than 40% larger than that delivered by LMTF (4 h) (101 mAh $g^{-1}$, Figure 4D). We also characterize the rate capability of LMTF (35 min) and LMTF (4 h) using a "slow-charge, fast discharge" protocol, i.e., charging both materials to a capacity of 250 mAh $g^{-1}$ at 20 mA $g^{-1}$, rest for 1 hour and then discharging at 20 mA $g^{-1}$, 500 mA $g^{-1}$, and 2 A $g^{-1}$, respectively (Fig. S7). With the same charge capacity, LMTF (35min) still demonstrates a comparable or larger discharge capacity in all rates, especially at a higher rate. Additional Galvanostatic intermittent titration (GITT) measurements of LMTF (35min) and LMTF (4h) were conducted, as presented in Figure S8, which confirm that LMTF (35min) generally has a lower overpotential and higher Li diffusivity than LMTF (4h). These results prove the success of the synthetic optimization strategy to shorten the sintering duration at high temperature, uncovered by systematically investigating the structural evolution of the material during the synthesis process. This enhancement in electrochemistry does not require any compositional modification and basically comes 'for free' as one only needs to keep the sample in the furnace for a shorter time, which potentially can increase throughput when cathode synthesis is scaled up.

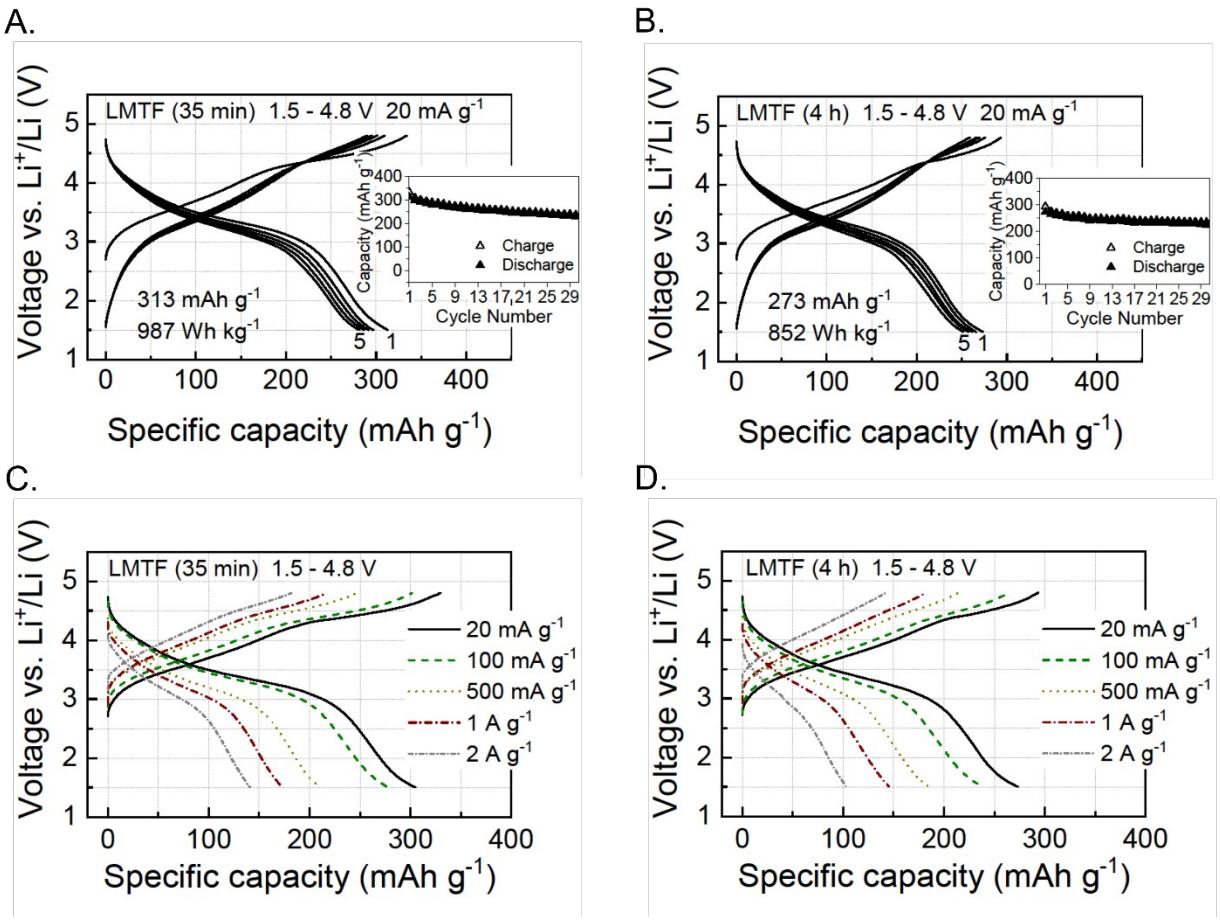


**Figure 4. Electrochemical performance of LMTF (35 min) and LMTF (4 h).** Voltage profiles and capacity retention of **(A)** LMTF (35 min) and **(B)** LMTF (4 h) within the voltage window of 1.5–4.8 V at 20 mA $g^{-1}$ and 25°C. Rate capability of **(C)** LMTF (35 min) and **(D)** LMTF (4 h): the first-cycle voltage profiles when cycled between 1.5 and 4.8 V at 20, 100, 500, 1000, and 2000 mA $g^{-1}$.

## 6. Outlook

The performance of functional materials often depends on minor details of their structure such as compositional inhomogeneities, point defects, or in the case presented here, short-range cation order. While computational modeling and high-resolution characterization techniques can be used to identify such structural features, controlling them in the production of materials is often difficult.

Recent advances to track the structural evolution via diffraction or spectroscopy techniques have started to provide a much more detailed picture of how compounds form [3, 5, 21], enabling targeted optimization of the synthesis protocol, such as wisely selecting suitable precursor sets, and accurately controlling the temperature and synthesis time to obtain metastable phases. This approach becomes even more instructive when combining synthetic optimization with functional enhancement, as demonstrated in this work. By tracking the detailed structural features of a multi-component oxyfluoride, especially the formation of SRO in DRX materials, we identify that unlike LRO, which forms rapidly and at a relatively low temperature, SRO evolves slowly at high temperature consistent with the very different energy scale associated with SRO and LRO. Taking advantage of this observation, we proposed a synthetic optimization strategy to quench the sample at an early stage of high-temperature sintering when LRO has formed without extensive SRO, creating a DRX material with enhanced capacity and rate capability. The SRO-optimized LMTF (35 min) sample exhibits a capacity of >310 mAh $g^{-1}$ and a specific energy close to 1000 Wh $kg^{-1}$ and enables discharge up to 2 A $g^{-1}$, making it a promising Li-ion cathode composed of only inexpensive and earth-abundant Mn and Ti.

We also believe such methodology of synthesis-induced functional improvement can be applied to other classes of functional materials and speed up the targeted optimization of their synthetic protocols and functional enhancement. For instance, in Ni-rich Ni–Mn–Co (NMC)-type Li-ion cathodes, the interlayer mixing between Li and Ni has been closely linked to the Li-transport and capacity degradation of the material, which is sensitive to the synthesis condition.[23] Systematic tracking of the Li/Ni mixing behavior upon synthesis may enable us to improve the synthesis protocol and mitigate such unfavorable cation mixing. Single-atom doping in 2D materials, such as graphene or $MoS_2$, has been proven effective to enhance certain functionalities such as catalytic activities.[24] *In situ* tracking of the incorporation of the dopant atoms during synthesis using local structural characterization techniques may provide useful insight for controlling the doping sites and concentration into the matrix and ultimately lead to improved functionalities. We are thus eager to see more of such functional optimization of ceramic materials assisted by "opening the black box" of synthesis.

## 7. Methods

*Synthesis and lab-based characterizations*: The LMTF compounds were synthesized using a traditional solid-state method with different sintering time. $Li_2CO_3$ (Alfa Aesar, ACS, 99% min), $Mn_2O_3$ (Alfa Aesar, 99.9%), $TiO_2$ (Alfa Aesar, 99.9%), and LiF (Alfa Aesar, 99.99%) were used as precursors. All the precursors were stoichiometrically mixed in ethanol with a Retsch PM 400 planetary ball mill at a rate of 180 rpm for 12 h. 15% excess $Li_2CO_3$ was added to compensate for possible loss during synthesis, especially during the 600°C-holding process. The precursors were then dried in an oven at 70°C overnight and pelletized. The precursor pellets were first heated to 600°C with Ar gas flow at a rate of 5 °C/min and held for 1 hour to decompose carbonate species. The pre-heated pellets were then covered with Ni foil and sealed in quartz tubes filled with Ar with an ampoule sealing system. The tubes were further heated to 1000°C at a rate of 5 °C/min, followed by different sintering time. This set up allows a more accurate control of the sintering time at 1000°C. The sealed tubes with wrapped pellets were quenched to room temperature at designated time, transferred to a glovebox, and ground into powders.

Lab XRD patterns were obtained using a Rigaku Miniflex 600 or Bruker D8 ADVANCE diffractometer (Cu source) in the $2\theta$ range of 15–90°. Rietveld refinement was performed using PANalytical X'pert HighScore Plus software. Elemental analysis was performed using direct current plasma emission spectroscopy (PerkinElmer Optima 5300 DV Optical Emission Spectrometer) for lithium, titanium, and manganese. SEM images were collected using a Zeiss Gemini Ultra-55 analytical field-emission SEM at the Molecular Foundry at Lawrence Berkeley National Lab (LBNL). Particle size analyses were performed by ImageJ, with more than 100 particles evaluated.

*Electrochemistry*: All the cathode films were free-standing and composed of the active materials, Super C65 (Timcal), and polytetrafluoroethylene (PTFE, DuPont, Teflon 8A) at a weight ratio of 60:30:10. To make the cathode films, 300 mg of the as-synthesized active materials and 150 mg of Super C65 were mixed and shaker-milled for 90 min in an argon atmosphere using a SPEX 800M mixer/mill. Additional XRD and TEM characterizations of LMTF (35min) and LMTF (4h) were conducted to discuss the structural change during the shaker mill process (Fig. S9, S10). PTFE was later added and manually mixed with the shaker-milled mixture for 40 min. The components were then rolled into thin films inside a glovebox. Commercial 1 M $LiPF_6$ in ethylene carbonate (EC) and dimethyl carbonate (DMC) solution (1:1 volume ratio) was used as the electrolyte. A glass microfiber filter (Whatman) was used as the separator. FMC Li metal foil was used as the anode. Coin cells were assembled inside the glovebox and tested on an Arbin battery test instrument at 25°C. The loading density of the films was approximately 3–4 mg $cm^{-2}$ based on the active materials. For the rate-capability tests, a smaller loading density of approximately 2.5 mg $cm^{-2}$ based on the active materials was used. The specific capacities were calculated based on the weight of active materials (60%) in the cathode films. For the GITT measurements, each step in the voltage profiles corresponds to a galvanostatic charge/discharge of 10 mAh $g^{-1}$ at a rate of 20 mA $g^{-1}$ followed by a 6 h relaxation step.

*TEM Characterization*: The high-angle annular dark-field scanning transmission electron microscopy (HAADF-STEM), energy dispersive spectroscopy and electron diffraction characterization for both *ex situ* and *in situ* experiments were performed using an FEI TitanX 60-300 microscope equipped with Bruker windowless EDX detector at an accelerating voltage of 300 KV in the Molecular Foundry at LBNL.

The *in situ* heating experiments were performed on a Protochips Fusion Select holder. The pre-heated LMTF pellet (600°C in Ar atmosphere for 1 hour) was grinded into fine powder, diluted in hexane, sonicated to obtain good particle dispersion, and then drop casted on a Protochips Fusion Thermal E-chip. The Thermal E-chips comprise a central conductive ceramic membrane supported by a silicon substrate. Nine 8-micron holes covered with ~18 nm holey carbon film were located in the center of the membrane to provide an electron transparent area for TEM imaging. Joule heating occurs when electrical current is forced across the conductive membrane. For *ex situ* characterization, the TEM samples were prepared by drop casting the dilute LMTF dispersion onto a standard 400 copper mesh TEM grid with lacey carbon support.

*Ex situ synchrotron XRD and PDF*: Synchrotron XRD and PDF measurements were performed at beamline 11-ID-B at the Advanced Photon Source (APS) of Argonne National Laboratory using a constant wavelength of 0.2115 Å. The sample-to-detector distances were 180 mm for PDF and 1000 mm for XRD. All *Ex situ* samples were packed into Kapton capillaries (Cole-Parmer) and sealed with epoxy in an Ar-filled glovebox. The total scattering data was integrated using GSAS-II software to obtain 1D XRD spectra and *G(r)* was obtained using xPDF suite package. A $CeO_2$ standard was used for calibration and to determine the instrumental parameters. PDF fitting was conducted using PDFGui software package. The PDF spectra were refined against a completely random DRX structure model with Fm-3m space group in a short *r*-range between 1.8 and 15 Å. Only scale factor, lattice constant (*a*), peak shape factor ($\delta_1^*$), and isotropic thermal displacement parameter ($U_{iso}$) were allowed to refine. $U_{iso}$ was constrained to be the same on the same lattice position. The site occupancies of different atoms were set to the target values and not refined.

*Computational methods*: A cluster expansion model has been constructed to produce the structure with SRO in the $Li_{1.2}Mn_{0.55}^{3+}Ti_{0.25}^{4+}O_{1.85}F_{0.15}$ compound. In such a cluster expansion, the configurational energy dependence is captured by an expansion into different cluster functions, which can be formulated as [25]:

$$E = \sum_{i,sp1} J_i^{sp1}\sigma_i^{sp1} + \sum_{i,j,sp1,sp2} J_{ij}^{sp1\,sp2}\sigma_i^{sp1}\sigma_j^{sp2} + \sum_{i,j,k,sp1,sp2,sp3} J_{ijk}^{sp1\,sp2\,sp3}\sigma_i^{sp1}\sigma_j^{sp2}\sigma_k^{sp3} \ldots\ldots$$

Here, $\sigma_i^{sp}$ corresponds to the occupancy of a certain site(s) with a certain species *sp* and *J* refers to the effective cluster interactions (ECIs).

In a DRX material, a cation site can be occupied by $Li^+$, $Mn^{3+}$ and $Ti^{4+}$ while the anion sites can be occupied by either $O^{2-}$ or $F^-$. For each system, pair interactions up to 7.1 Å, triplet interactions up to 4.0 Å, and quadruplet interactions up to 4.0 Å based on a rocksalt lattice with a cubic lattice parameter $a$ = 3.0 Å were included in the cluster-expansion formalism. The ECIs were fitted to DFT energies of sampled structures using a L1-regularized least-squares regression approach[26], with the regularization parameters selected to minimize cross-validation error [26, 27]. The DFT results of 1251 structures are applied to fit the cluster expansion, which end up with a cluster expansion model that has root-mean-squared error of 7.53 meV/atom.

Special quasi-random structures (SQSs) are periodic structures whose atomic distributions are selected such that the cluster correlations approach the expected value in a random atomic arrangement as closely as possible for a given structure size[28]. Given this feature, SQSs are an appropriate choice to investigate the properties of rocksalt materials with full disorder. In the

alloy community, for example, SQSs have been successfully used to evaluate mixing enthalpies[29] and to model the electronic structure of random alloys[30]. Our previous studies on DRXs using SQS structures also indicate that these structures can be effective tools for quantifying the phase stability[31], electronic structure[32], and voltage curves[33]. To model the random cation distribution of the fully disordered rocksalt materials, we generated SQS structures for the example composition, i.e., $Li_{1.2}Mn_{0.55}^{3+}Ti_{0.25}^{4+}O_{1.85}F_{0.15}$, with a 2×4×5 supercell of rocksalt primitive cell (80 atoms).

First-principles density functional theory (DFT) calculations were performed to obtain an accurate description of the structural energies and oxidation states of the different cathode materials. All the calculations were performed using the projector-augmented wave (PAW) method[34] as implemented in the Vienna Ab initio Simulation Package (VASP)[35]. A rotationally averaged Hubbard U correction[36, 37] was used to correct the self-interaction error on the transition metals in the compound. The U parameters were obtained from a previously reported calibration to oxide formation energies[37]. For all the calculations, a reciprocal space discretization of 25 k-points per $Å^{-1}$ was applied, and the convergence criteria were set as $10^{-6}$ eV for electronic loops and 0.02 eV $Å^{-1}$ for ionic loops. The reaction energy is normalized by the cation amount.

## Supporting Information

Supporting Information is available from the Wiley Online Library or from the author.


## Acknowledgements

This work was supported by the U.S. Department of Energy, Office of Science, Basic Energy Sciences, Materials Sciences and Engineering Division under Contract No. DE-AC02-05-CH11231 within the [GENESIS EFRC] program [DE-SC0019212]. Work at the Molecular Foundry was supported by the Office of Science, Office of Basic Energy Sciences, of the U.S. Department of Energy under contract No. DE-AC02-05CH11231. This research used resources of the Advanced Photon Source, an Office of Science User Facility operated for the U.S. Department of Energy (DOE) Office of Science by Argonne National Laboratory, and was supported by the U.S. DOE under Contract No. DE-AC02-06CH11357. The computational analysis was performed using computational resources sponsored by the Department of Energy's Office of Energy Efficiency and Renewable Energy and located at the National Renewable Energy Laboratory, computational resources provided by Extreme Science and Engineering Discovery Environment (XSEDE), which was supported by National Science Foundation grant number ACI1053575, as well as the National Energy Research Scientific Computing Center (NERSC), a DOE Office of Science User Facility supported by the Office of Science and the U.S. Department of Energy under Contract No. DE-AC02-05CH11231. The authors thank Protochips Inc. for assistance with the *in situ* TEM heating stage schematic demonstration figure (Fig. 1A).

**Author information**

These authors contributed equally: Zijian Cai, Ya-Qian Zhang, Zhengyan Lun.

**Author contributions**

Z. L. conceived the idea and planned the project with M. C. S. and G. C.; G. C. supervised all aspects of this research; Z. C. and Z. L. designed the synthesis protocol, synthesized, characterized, and electrochemically tested the compounds with help from H. -M. H. and Y. C.; Y.-Q. Z. acquired and analyzed TEM and SEM data with the input from M. C. S.; B. O. performed all the calculations and analyzed the data; L. C. G. acquired the synchrotron XRD and PDF data; Z. L. and Z. C. analyzed the synchrotron XRD and PDF data; Z.C. and Y.S. conducted ICP measurement, additional SEM measurement and performed the particle size analysis; The manuscript was written by Z. L., Z. C., and G. C., and was revised by all other authors. All authors approved the manuscript and contributed to discussions.

**Data availability**

All relevant data within the article are available from the corresponding authors upon reasonable request.

**Corresponding authors**

Correspondence to Zhengyan Lun, Mary C. Scott, and Gerbrand Ceder.

**Competing interests**

The authors declare no competing interests

**References**

[1] J.-O. Andersson, T. Helander, L. Höglund, P. Shi, B. Sundman, Calphad 2002, 26, 273; S. P. Ong, L. Wang, B. Kang, G. Ceder, Chemistry of Materials 2008, 20, 1798; J. Sopoušek, A. Kryštofová, M. Premović, O. Zobač, S. Polsterová, P. Brož, J. Buršík, Calphad 2017, 58, 25; D. A. Kitchaev, Z. Lun, W. D. Richards, H. Ji, R. J. Clément, M. Balasubramanian, D.-H. Kwon, K. Dai, J. K. Papp, T. Lei, Energy & Environmental Science 2018, 11, 2159.
[2] D. P. Shoemaker, Y.-J. Hu, D. Y. Chung, G. J. Halder, P. J. Chupas, L. Soderholm, J. F. Mitchell, M. G. Kanatzidis, Proceedings of the National Academy of Sciences 2014, 111, 10922; Y. Duan, L. Yang, M.-J. Zhang, Z. Chen, J. Bai, K. Amine, F. Pan, F. Wang, Journal of Materials Chemistry A 2019, 7, 513.
[3] A. J. Martinolich, J. R. Neilson, Chemistry of Materials 2017, 29, 479; P. K. Todd, M. J. McDermott, C. L. Rom, A. A. Corrao, J. J. Denney, S. S. Dwaraknath, P. G. Khalifah, K. A. Persson, J. R. Neilson, Journal of the American Chemical Society 2021, 143, 15185.
[4] M. Bianchini, J. Wang, R. J. Clément, B. Ouyang, P. Xiao, D. Kitchaev, T. Shi, Y. Zhang, Y. Wang, H. Kim, Nature materials 2020, 19, 1088.
[5] A. Miura, C. J. Bartel, Y. Goto, Y. Mizuguchi, C. Moriyoshi, Y. Kuroiwa, Y. Wang, T. Yaguchi, M. Shirai, M. Nagao, Advanced Materials 2021, 2100312.
[6] J. Lee, A. Urban, X. Li, D. Su, G. Hautier, G. Ceder, Science 2014, 343, 519.
[7] N. Yabuuchi, M. Takeuchi, M. Nakayama, H. Shiiba, M. Ogawa, K. Nakayama, T. Ohta, D. Endo, T. Ozaki, T. Inamasu, Proceedings of the National Academy of Sciences 2015, 112, 7650.
[8] N. Yabuuchi, The Chemical Record 2019, 19, 690.
[9] R. J. Clément, Z. Lun, G. Ceder, Energy & Environmental Science 2020, 13, 345.
[10] X. Fu, D. N. Beatty, G. G. Gaustad, G. Ceder, R. Roth, R. E. Kirchain, M. Bustamante, C. Babbitt, E. A. Olivetti, Environmental Science & Technology 2020, 54, 2985.
[11] J. Reed, G. Ceder, Chemical reviews 2004, 104, 4513.
[12] A. Urban, J. Lee, G. Ceder, Advanced Energy Materials 2014, 4, 1400478.
[13] W. H. Kan, B. Deng, Y. Xu, A. K. Shukla, T. Bo, S. Zhang, J. Liu, P. Pianetta, B.-T. Wang, Y. Liu, Chem 2018, 4, 2108; N. Mozhzhukhina, J. Kullgren, C. Baur, O. Gustafsson, W. R. Brant, M. Fichtner, D. Brandell, Journal of Raman Spectroscopy 2020, 51, 2095.
[14] H. Ji, A. Urban, D. A. Kitchaev, D.-H. Kwon, N. Artrith, C. Ophus, W. Huang, Z. Cai, T. Shi, J. C. Kim, Nature communications 2019, 10, 592.
[15] B. Ouyang, N. Artrith, Z. Lun, Z. Jadidi, D. A. Kitchaev, H. Ji, A. Urban, G. Ceder, Advanced Energy Materials 2020, 10, 1903240.
[16] H. Ji, J. Wu, Z. Cai, J. Liu, D.-H. Kwon, H. Kim, A. Urban, J. K. Papp, E. Foley, Y. Tian, M. Balasubramanian, H. Kim, R. J. Clément, B. D. McCloskey, W. Yang, G. Ceder, Nature Energy 2020, 5, 213.

[17] Z. Lun, B. Ouyang, D.-H. Kwon, Y. Ha, E. E. Foley, T.-Y. Huang, Z. Cai, H. Kim, M. Balasubramanian, Y. Sun, Nature materials 2021, 20, 214.
[18] R. De Ridder, G. Van Tendeloo, S. Amelinckx, Acta Crystallographica Section A: Crystal Physics, Diffraction, Theoretical and General Crystallography 1976, 32, 216.
[19] N. Yabuuchi, M. Nakayama, M. Takeuchi, S. Komaba, Y. Hashimoto, T. Mukai, H. Shiiba, K. Sato, Y. Kobayashi, A. Nakao, Nature communications 2016, 7, 13814; Z. Lun, B. Ouyang, D. A. Kitchaev, R. J. Clément, J. K. Papp, M. Balasubramanian, Y. Tian, T. Lei, T. Shi, B. D. McCloskey, Advanced Energy Materials 2019, 9, 1802959.
[20] P. J. Chupas, K. W. Chapman, C. Kurtz, J. C. Hanson, P. L. Lee, C. P. Grey, Journal of Applied Crystallography 2008, 41, 822.
[21] A. Miura, H. Ito, C. J. Bartel, W. Sun, N. C. Rosero-Navarro, K. Tadanaga, H. Nakata, K. Maeda, G. Ceder, Materials horizons 2020, 7, 1310; M. J. McDermott, S. S. Dwaraknath, K. A. Persson, Nature communications 2021, 12, 1.
[22] Z. Lun, B. Ouyang, Z. Cai, R. J. Clément, D.-H. Kwon, J. Huang, J. K. Papp, M. Balasubramanian, Y. Tian, B. D. McCloskey, Chem 2020, 6, 153.
[23] C. Xu, P. J. Reeves, Q. Jacquet, C. P. Grey, Advanced Energy Materials 2021, 11, 2003404; E. D. Orlova, A. A. Savina, S. A. Abakumov, A. V. Morozov, A. M. Abakumov, Symmetry 2021, 13, 1628.
[24] X. Zhang, J. Guo, P. Guan, C. Liu, H. Huang, F. Xue, X. Dong, S. J. Pennycook, M. F. Chisholm, Nature communications 2013, 4, 1; J. Deng, H. Li, J. Xiao, Y. Tu, D. Deng, H. Yang, H. Tian, J. Li, P. Ren, X. Bao, Energy & Environmental Science 2015, 8, 1594; Z. Li, Y. Chen, S. Ji, Y. Tang, W. Chen, A. Li, J. Zhao, Y. Xiong, Y. Wu, Y. Gong, Nature chemistry 2020, 12, 764.
[25] J. M. Sanchez, F. Ducastelle, D. Gratias, Physica A: Statistical Mechanics and its Applications 1984, 128, 334; C. Wolverton, D. de Fontaine, Physical Review B 1994, 49, 8627.
[26] L. J. Nelson, G. L. W. Hart, F. Zhou, V. Ozoliņš, Physical Review B 2013, 87, 035125.
[27] Z. Lun, B. Ouyang, Z. Cai, R. J. Clément, D.-H. Kwon, J. Huang, J. K. Papp, M. Balasubramanian, Y. Tian, B. D. McCloskey, H. Ji, H. Kim, D. A. Kitchaev, G. Ceder, Chem 2019; B. Ouyang, N. Artrith, Z. Lun, Z. Jadidi, D. A. Kitchaev, H. Ji, A. Urban, G. Ceder, Advanced Energy Materials 2020, 10, 1903240; D. A. Kitchaev, Z. Lun, W. D. Richards, H. Ji, R. J. Clément, M. Balasubramanian, D.-H. Kwon, K. Dai, J. K. Papp, T. Lei, B. D. McCloskey, W. Yang, J. Lee, G. Ceder, Energy & Environmental Science 2018, 11, 2159; W. D. Richards, S. T. Dacek, D. A. Kitchaev, G. Ceder, Advanced Energy Materials 2018, 8, 1701533; H. Ji, D. A. Kitchaev, Z. Lun, H. Kim, E. Foley, D.-H. Kwon, Y. Tian, M. Balasubramanian, M. Bianchini, Z. Cai, R. J. Clément, J. C. Kim, G. Ceder, Chemistry of Materials 2019, 31, 2431.
[28] A. Zunger, S. H. Wei, L. G. Ferreira, J. E. Bernard, Physical Review Letters 1990, 65, 353.
[29] D. Shin, A. van de Walle, Y. Wang, Z.-K. Liu, Physical Review B 2007, 76, 144204.

[30] S. H. Wei, L. G. Ferreira, J. E. Bernard, A. Zunger, Physical Review B 1990, 42, 9622.
[31] A. Urban, I. Matts, A. Abdellahi, G. Ceder, Advanced Energy Materials 2016, 6, 1600488.
[32] A. Urban, A. Abdellahi, S. Dacek, N. Artrith, G. Ceder, Physical review letters 2017, 119, 176402.
[33] A. Abdellahi, A. Urban, S. Dacek, G. Ceder, Chemistry of Materials 2016, 28, 3659; A. Abdellahi, A. Urban, S. Dacek, G. Ceder, Chemistry of Materials 2016, 28, 5373.
[34] G. Kresse, D. Joubert, Physical Review B 1999, 59, 1758.
[35] G. Kresse, J. Furthmüller, Computational Materials Science 1996, 6, 15.
[36] S. L. Dudarev, G. A. Botton, S. Y. Savrasov, C. J. Humphreys, A. P. Sutton, Physical Review B 1998, 57, 1505.
[37] L. Wang, T. Maxisch, G. Ceder, Physical Review B 2006, 73, 195107.